



1 **Improved Atmospheric Characterization through Fused Mobile**  
2 **Airborne & Surface *In Situ* Surveys: Methane Emissions**  
3 **Quantification from a Producing Oil Field**

4 Ira Leifer<sup>1</sup>, Christopher Melton<sup>1</sup>, Marc L. Fischer<sup>2</sup>, Matthew Fladeland<sup>3</sup>, Jason Frash<sup>1</sup>, Warren Gore<sup>3</sup>,  
5 Laura Iraci<sup>3</sup>, Josette Marrero<sup>3</sup>, Ju-Mee Ryoo<sup>3</sup>, Tomoaki Tanaka<sup>3</sup>, Emma Yates<sup>3</sup>

6 <sup>1</sup>Bubbleology Research International, Solvang, CA 93463, [ira.leifer@bubbleology.com](mailto:ira.leifer@bubbleology.com)

7 <sup>2</sup>Lawrence Berkeley National Laboratory, 1 Cyclotron Road, Berkeley CA 94720.

8 <sup>3</sup>NASA Ames Research Center, Moffett Field, CA, 94035

9  
10 **Correspondence to:** Ira Leifer ([Ira.Leifer@bubbleology.com](mailto:Ira.Leifer@bubbleology.com))

11  
12 **Abstract.** Methane (CH<sub>4</sub>) inventory uncertainties are large, requiring robust emission derivation  
13 approaches. We report on a fused airborne/surface data collection approach to derive emissions from an  
14 active oil field near Bakersfield, central California. The approach characterizes the atmosphere from the  
15 surface to above the planetary boundary layer (PBL) and combines downwind trace gas concentration  
16 anomaly (plume) above background with normal winds to derive flux. This approach does not require a  
17 well-mixed PBL, allows explicit, data based, uncertainty evaluation, and was applied to complex  
18 topography and wind flows.

19  
20 *In situ* airborne (collected by AJAX – the Alpha Jet Atmospheric eXperiment) and mobile surface  
21 (collected by AMOG – the AutoMOBILE trace Gas – Surveyor) data were collected on 19 August 2015 to  
22 assess source strength. Data included an AMOG and AJAX intercomparison transect profiling from the  
23 San Joaquin Valley (SJV) floor into the Sierra Nevada Mountains (0.1-2.2 km altitude), validating a novel  
24 surface approach for atmospheric profiling by leveraging topography. The profile intercomparison found  
25 good agreement in multiple parameters for the overlapping altitude range from 500 to 1500 m, for the  
26 upper 5% of surface winds, which accounts for wind-impeding structures, i.e., terrain, trees, buildings,  
27 etc. Annualized emissions from the active oil fields were 31.3±16 Gg methane and 2.4±1.2 Tg carbon  
28 dioxide. Data showed the PBL was not well-mixed at distances of 10-20 km downwind, highlighting the  
29 importance of the experimental design.

30



## 31 1. Introduction

### 32 1.1. Methane Trends and Uncertainty

33 On decadal timescales, methane ( $\text{CH}_4$ ), affects the atmospheric radiative balance more strongly than  
34 carbon dioxide ( $\text{CO}_2$ ) (IPCC, 2007, Fig. 2.21). Since pre-industrial times,  $\text{CH}_4$  emissions have risen by a  
35 factor of 2.5 (Khalil and Rasmussen, 1995), while estimates of its lifetime has decreased and now is  
36 estimated at  $\sim 8.5$  years (Sonnemann and Grygalashvyly, 2014). Atmospheric  $\text{CH}_4$  growth almost ceased  
37 between 1999 and 2006, but has resumed since 2007 (Nisbet et al., 2015). Several processes are proposed  
38 to underlie this trend (Ghosh et al., 2015; John et al., 2012; Nisbet et al., 2015); however, high uncertainty  
39 in emission inventories (IPCC, 2013) complicates interpretation of the underlying mechanism(s).

40

41 The dominant  $\text{CH}_4$  loss arises from reaction with hydroxyl (OH), whose concentration has been  
42 increasing in recent decades (John et al., 2012), causing a decrease in the estimated  $\text{CH}_4$  lifetime of  $0.5\%$   
43  $\text{yr}^{-1}$  (Karlsdóttir and Isaksen, 2000). Overall, the estimate of the  $\text{CH}_4$  lifetime has decreased by  $\sim 40\%$  from  
44 an estimated 12 years in 2007 (IPCC, 2007). The recent discovery of a new significant  $\text{CH}_4$  loss  
45 mechanism, terrestrial uptake (Fernandez-Cortes et al., 2015), illustrates the need to understand loss  
46 mechanisms better.

47

48 Large  $\text{CH}_4$  budget uncertainties remain for many sources (IPCC, 2013), with greater uncertainty in future  
49 trends from global warming feedback (Rigby et al., 2008) and increasing anthropogenic activities  
50 (Kirschke et al., 2013; Wunch et al., 2009). Emphasizing these uncertainties are recent studies that  
51 suggest underestimation by a factor of 1.5 in the important anthropogenic  $\text{CH}_4$  source, Fossil Fuel  
52 Industrial (FFI) emissions (Brandt et al., 2014). Tellingly, this discrepancy only was noted recently  
53 (Miller et al., 2013), in part because the US  $\text{CH}_4$  monitoring network is too sparse to constrain emissions  
54 at “regional to national scales” (Dlugokencky et al., 2013). FFI emissions are the most (Brandt et al.,  
55 2014; EPA, 2017) anthropogenic contributor to the global  $\text{CH}_4$  budget. Whereas EPA inventory values  
56 and Bruhwiler et al. (2017) suggest no significant trends in the north American emissions over the last  
57 decade, satellite and surface observations suggest a 30% increase in US  $\text{CH}_4$  emissions (Turner et al.,  
58 2016). However, Turner et al. (2016) could not ascribe a specific source. These uncertainties strongly  
59 argue for the need for new, robust methodologies for flux derivation.



## 60 1.2. Methane Flux Estimation

61 Various approaches have been developed to derive surface emissions from CH<sub>4</sub> concentration  
62 measurements including direct assessment (Peischl et al., 2015; White et al., 1976), data-driven mass  
63 balance, e.g., Karion et al. (2013), tracer-tracer ratio (LaFranchi et al., 2013), and assimilation inverse  
64 models, e.g. Jeong et al. (2013); Jeong et al. (2012). Challenges for the latter approach include the needs  
65 for accurate meteorological transport models and good *a priori* emission distributions (Miller et al.,  
66 2013). Miller et al. (2013) concluded that bottom-up inventories (EPA, 2013; European Commission,  
67 2010) significantly underestimate husbandry and FFI emissions. To apportion CH<sub>4</sub> to FFI versus  
68 biological sources, the tracer-tracer approach has been applied using ethane, whose emission ratio to CH<sub>4</sub>  
69 requires tight constraint (Peischl et al., 2013; Simpson et al., 2012; Wennberg et al., 2012). In practice,  
70 this emission ratio is an *a priori* assumption in the approach.

71

72 Direct assessment approaches have advantages over inversion approaches. Direct approaches allow  
73 explicit uncertainty evaluation and do not require an *a priori* emission spatial distribution, which may be  
74 unknown. Direct approaches also do not require the ability to model atmospheric transport accurately  
75 across the study region. In areas of complex topography or highly variable winds, this transport can  
76 challenge assimilation approaches, which also are challenged in areas with poorly characterized (or  
77 unknown) or highly variable sources, particularly if the measurement network is sparse. For direct  
78 assessment approaches, data collection should be rapid if winds and/or emissions are variable, and at  
79 adequate data density to characterize fine-scale structure.

## 80 1.3. Study Motivation

81 Herein we report on a novel application of fused airborne and surface *in situ* data to directly estimate CH<sub>4</sub>  
82 emissions. Specifically, on 19 August 2015, NASA's Alpha Jet Atmospheric eXperiment (AJAX)  
83 collected 1164 km of airborne data while AMOG (AutoMOBILE greenhouse Gas) Surveyor collected 1074  
84 km of contemporaneous mobile surface data. Both measure carbon dioxide (CO<sub>2</sub>), CH<sub>4</sub>, water vapor  
85 (H<sub>2</sub>O), and ozone (O<sub>3</sub>), as well as winds, pressure, relative humidity (*RH*), and temperature (*T*). These  
86 surface and airborne datasets were collected in a downwind curtain or plane oriented approximately  
87 orthogonal to the winds, to characterize the full planetary boundary layer (PBL) from surface to above the  
88 PBL. Additionally, the survey route was designed to include an ascent to ~2.2 km above sea level to  
89 include surface PBL characterization. Data fusion between platforms was validated by a vertical profile  
90 intercomparison for 0.5 to 1.5 km altitude by AMOG SURVEYOR leveraging topographic relief.  
91 Leveraging topographic relief –mountainous terrain affects about half the earth's population and about



92 half the earth's land surface (Meyers and Steenburgh, 2013) – allows a surface platform to collect  
93 atmospheric profile data and is a useful research tool in the absence of airborne resources.

#### 94 **1.4 The South San Joaquin Valley, California**

95 Most of California oil production lies in the San Joaquin Valley (SJV), as does most of California  
96 agriculture, including many intensive dairies (Gentner et al., 2014), and the major north-south  
97 transportation artery. For this study, data were collected for the Kern River oil fields (Kern Front oil field,  
98 Kern River oil field and the Poso Creek oil field, referred to herein as the Kern Fields), located adjacent to  
99 northwest Bakersfield (**Fig. 1A**). These adjacent oil fields create a strong CH<sub>4</sub> source that largely is  
100 isolated from confounding plumes from other SJV sources. This area includes complex wind flow  
101 patterns across and around the “toe” of Sierra Nevada Mountain foothills, which extend into the Kern  
102 Front and Kern River oil fields. Here, topographic steering ensures predictable prevailing northwesterly  
103 winds blow across the Kern Fields.

104 Strong orographic forcing also arises from tall bluffs (~100 m) on the Kern River Valley's south bank,  
105 which also separates the Kern River oil field from the urban city of Bakersfield (pop. 364,000 in 2013).  
106 The fine-scale wind structure that results from orographic forcing on transport dictated an anomaly  
107 approach for flux derivation, as did the presence of strong CH<sub>4</sub> structures (plumes) in the valley's lowest  
108 air. In the anomaly approach, transects must extend beyond a reasonably well-defined plume.

109

110 Topography (i.e., mountain ranges) plays a locally dominant role in overall southern California air flows  
111 where upper level winds locally force the lower level flows that transport pollutants (Bao et al., 2008).  
112 The SJV is delimited on the east by the Sierra Nevada Mountains and on the west by the Transverse  
113 Coastal Mountain Range (**Fig. 1A**). Transport between the SJV and adjacent air basins is poor due to  
114 California's mountain ranges. The SJV features weak surface winds (Bao et al., 2008) with the worst air  
115 quality in the United States occurring in the cities of Bakersfield and Delano (American Lung  
116 Association, 2016) in the SJV.

117

118 Pacific Ocean air primarily enters the SJV through the San Francisco Bay area and the Carquinez Strait,  
119 where it splits north into the Sacramento Valley and south into the SJV (Zhong et al., 2004). This flow  
120 extends up to ~1 km altitude. These winds are near orthogonal to the 600-km long central valley of  
121 California - i.e., cross-slope. South of Bakersfield, winds shift to from the west due to mountains that  
122 guide SJV air out into the Mojave Desert, where it affects air quality for up to hundreds of kilometers  
123 distance (VanCuren, 2015). Although the Tehachapi Pass is the main exit pathway of SJV air, other  
124 passes also transport air into the Mojave Desert. These flows are augmented by high inland temperatures

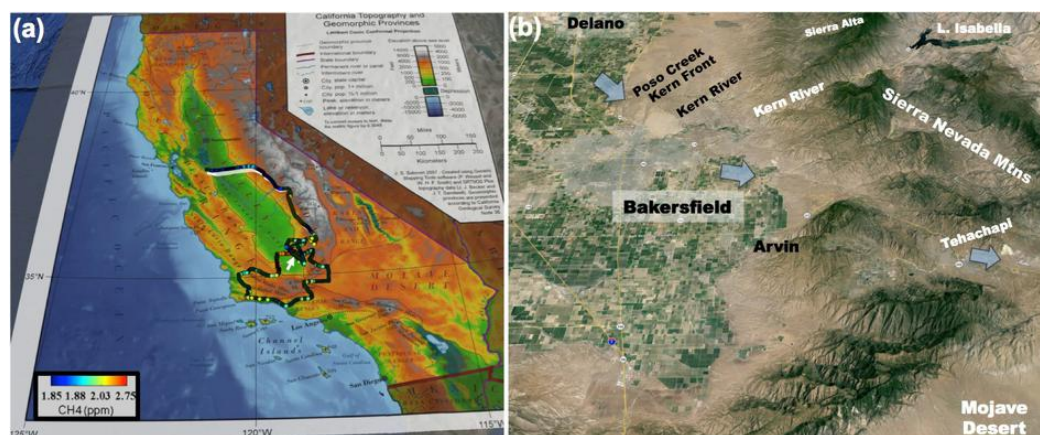


125 relative to the Pacific Ocean, which creates a horizontal pressure gradient that drives local upslope flows  
126 during the day and returning downslope nocturnal flows (Zhong et al., 2004). The pressure gradient is  
127 maximal around sunset, although winds peak ~4 hours later, shortly before midnight. This pressure  
128 gradient is controlled by the semi-permanent Pacific high, situated offshore central California, which  
129 diverts storms far to the north during summer. This pressure feature drives prevailing west-southwesterly  
130 winds at the regional scale in the California south coast air basins (Boucouvala and Bornstein, 2003).

## 131 2. Methodology

### 132 2.1. Experimental design

133 Data were collected as part of the *GOSAT-COMEX Experiment* (Greenhouse gases Observing SATellite -  
134 CO<sub>2</sub> and Methane Experiment - GCE) Campaign. GCE was developed to characterize emissions on  
135 spatial scales from decameter (*in situ* surface, imaging spectroscopy) to kilometer (*in situ* airborne) to  
136 deca-kilometer (satellite) in an area of complex topography. GCE design combined *in situ* mobile surface  
137 and airborne data with GOSAT satellite data. *In situ* data serve to assess the satellite pixel / plume  
138 overlap. Key GCE requirements are relatively steady, strong, isolated emissions and predictable and  
139 steady winds. Prevailing study area winds are from the west-northwest, veering to westerly winds to the  
140 southeast of Bakersfield (**Fig. 1**). Prevailing wind directions are highly reliable due to topographic  
141 control.



142  
143 **Figure 1.** (a) Full surface and airborne data for 19 Aug. 2015 mapped over California topography. White  
144 arrow shows Bakersfield. Data key on panel. (b) Study area map showing direction of prevailing winds  
145 and nearby mountain topography (Google Earth, 2016). See Supp. Fig. S1 for a high-altitude (20-km)  
146 photo of the entire study area and surrounding terrain.



147 GCE developed from the COMEX Campaign (Krautwurst et al., 2016), which combined *in situ* airborne  
148 and surface observations with both imaging and non-imaging spectroscopy to explore synergies for GHG  
149 emission estimation (Thompson et al., 2015). COMEX focused on southern California CH<sub>4</sub> sources  
150 including husbandry, landfills, natural geology, and petroleum hydrocarbon refining and production.

151

152 GCE combines airborne and surface data collected at dramatically different speeds. AJAX collects data at  
153 ~500 km hr<sup>-1</sup>, capturing a snapshot of atmospheric winds and plume structure. Surface GCE data are  
154 collected quasi-Lagrangian, starting northwest (upwind) and proceeding southeast and then east  
155 (downwind). This enables useful data collection even when a CH<sub>4</sub> plume drifts into the study area after  
156 the upwind survey – data collection proceeds downwind faster than advection. The surface route was  
157 designed carefully to traverse all targeted GOSAT pixels using rarely used (low traffic) surface roads and  
158 requires ~100 minutes.

159

160 Airborne and surface surveys are timed so that the downwind data plane (Krings et al., 2011) is surveyed  
161 concurrent with the satellite overpass. Data planes extend from the surface (AMOG) to above the PBL  
162 (AJAX), reducing uncertainty by providing a more complete atmospheric characterization including  
163 below where airplanes are permitted to fly (~500 m in an urban area). AJAX and AMOG profile data are  
164 fused to impose vertical structure during interpolation. Surface and airborne datasets are interpolated and  
165 fused to derive the flux passing through the data curtain (Sect. 2.5).

166

167 CGE first incorporates an upwind transit from Delano (100 m) on the SJV floor to Sierra Alta (1800 m)  
168 and higher to confirm that stranded CH<sub>4</sub> clouds (plumes disconnected from a source) do not threaten to  
169 impact the study area during the experiment, otherwise the survey is aborted. A key mission abort  
170 criterion is wind compliance. Specifically, winds must not be too light or variable, must flush nocturnal  
171 accumulations before the GOSAT overpass, and must be prevailing. The upwind transit provides vertical  
172 profile information including PBL height and vertical structure.

## 173 **2.2. AutoMOBILE trace Gas (AMOG) Surveyor**

174 Mobile atmospheric surface measurements have been conducted for many years using a customized van  
175 (Lamb et al., 1995) or a recreational vehicle (Farrell et al., 2013; Leifer et al., 2013). Recently, the  
176 development of cavity enhanced absorption spectroscopy (CEAS) analyzers has opened the way for rapid  
177 and highly accurate trace gas measurements (Leen et al., 2013) without the need for compressed gases as  
178 in gas chromatography (Farrell et al., 2013). This allows for smaller vehicle survey platforms at lower  
179 logistical overhead (Leifer et al., 2014; McKain et al., 2015; Pétron et al., 2012; Yacovitch et al., 2015). A



180 competing sensor technology that has been used in mobile survey data collection is open path  
181 spectroscopy (Sun et al., 2014). Older technology using fluorescence also can be incorporated onto  
182 mobile survey platforms, for example, to measure ozone, O<sub>3</sub>.

183

184 Mobile surface data were collected by the AMOG Surveyor (Leifer et al., 2014) (see Supp. Sect. S2.1 for  
185 additional details), a modified commuter car. AMOG Surveyor provides mobile high-speed, high-spatial  
186 resolution observations of meteorology (winds, temperature, pressure), trace gases (greenhouse and  
187 others), and remote sensing parameters. AMOG uses a range of trace gas analyzers and careful design  
188 with respect to wind flow around the vehicle to characterize strong spatial heterogeneity at up to highway  
189 speeds.

190

191 Two-dimensional winds are measured by a sonic anemometer (VMT700, Vaisala) mounted 1.4 m above  
192 the roof, above vehicle flow streamlines for slow to highway speeds. Air is drawn down two sample lines  
193 from 5 and 3 m above ground by a high-flow vacuum pump (GVB30, Edwards Vacuum) that feeds  
194 several gas analyzers. The greenhouse gases, CO<sub>2</sub>, CH<sub>4</sub>, and H<sub>2</sub>O, are measured at up to 10 Hz by an  
195 analyzer that uses Integrated Cavity Offaxis Spectrometer-Cavity Enhanced Absorption Spectroscopy  
196 (ICOS-CEAS, 911-0010, Los Gatos Research, Inc.). A fluorescence analyzer measured O<sub>3</sub> at 0.25 Hz  
197 (49C, ThermoFischer Scientific, MA). AMOG Surveyor's full trace gas suite (carbonyl sulfide, carbon  
198 monoxide, nitric oxide, nitrogen dioxide, hydrogen sulfide, sulfur dioxide, total sulfur, ammonia) was not  
199 deployed on 19 Aug. 2015.



200

201 **Figure 2.** Study platforms. (a) AutoMOBILE trace Gas (AMOG) Surveyor, Kern River oil field in  
202 background. Photo courtesy Ira Leifer. (b) The Alpha Jet Atmospheric eXperiment (AJAX) aircraft, photo  
203 courtesy Akihiko Kuze, JAXA. See Supplemental Material Section 1 for further details.

204 Relevant recent AMOG Surveyor improvements since Leifer et al. (2014) include a high speed  
205 thermocouple (50416-T, Cooper-Atkins) and a high accuracy (0.2 hPa) pressure sensor (61320V RM



206 Young Co.). Both are mounted in a roof passive radiation shield (7710, Davis Instruments) to largely  
207 eliminate dynamic pressure effects from the airflow. Position information is critical to accurate wind  
208 measurements and is provided by redundant (two) Global Navigation Satellite Systems (19X HVS,  
209 Garmin) that use the GLONASS, GPS, Galileo, and QZSS satellites at 10 Hz (WGS84). AMOG  
210 analyzers and sensor data are logged asynchronously on a single computer. Custom software integrates  
211 the data streams and provides real-time visualization of multiple parameters in the Google Earth  
212 environment.

### 213 **2.3. Alpha Jet Atmospheric eXperiment (AJAX)**

214 AJAX (Fig. 2b) collected airborne *in situ* measurements of CO<sub>2</sub>, CH<sub>4</sub>, H<sub>2</sub>O by cavity ring down  
215 spectroscopy (G2301-m, Picarro Inc.), O<sub>3</sub>, (Model 205, 2B Technologies Inc.), and meteorological  
216 parameters including 3D winds (Meteorological Measurement System). The greenhouse gas analyzer is  
217 calibrated using NOAA whole-air standards; calibrations are performed before and/or after each flight  
218 with the calibration factor closest to the day of flight being applied to each raw CO<sub>2</sub> and CH<sub>4</sub>  
219 measurement. Further corrections include applying water vapor corrections provided by Chen et al.  
220 (2010) to calculate CO<sub>2</sub> and CH<sub>4</sub> dry mixing ratios. Data also are filtered for quality control for deviations  
221 in instrument cavity pressure, to improve inflight precision.

222

223 The overall CH<sub>4</sub> measurement uncertainty is typically <2.2 ppb, including contributions from accuracy of  
224 the standard, precision (1- $\sigma$  over 6 min), calibration repeatability, inflight variance due to cavity pressure  
225 fluctuations, and uncertainty due to water corrections and pressure dependence (based on environmental  
226 chamber studies). See Hamill et al. (2015); Tanaka et al. (2016), and Yates et al. (2013) for further  
227 aircraft and instrumentation details, and Supp. Sect. S2.2.

### 228 **2.4. Background estimation and data fusion**

229 The flux ( $Q(x, z)$ ) with respect to lateral transect distance ( $x$ ) and altitude ( $z$ ) through the  $x, z$  plane is the  
230 product of the normal winds ( $U_n(x, z)$ ) and the plume concentration anomaly ( $C'(x, z)$ ). Interpolation of  $C'$   
231 and  $U_N$  is linear within the PBL and is assumed uniform above the PBL.

232

233 To calculate  $Q(x, z)$  requires  $C'$  relative to background ( $C_B(x, z)$ ), which is derived from evaluating  
234  $C_B(x < x_{max}/2, z)$  and  $C_B(x > x_{max}/2, z)$ , denoted  $C_{BL}(z)$  and  $C_{BR}(z)$ , respectively, where  $x_{max}$  is the lateral extent  
235 of the data curtain. Then,  $C_B(x, z)$  is derived from a linear polynomial fit of  $C_{BL}(z)$  and  $C_{BR}(z)$ .

236





237 Both  $C_{BL}(z)$  and  $C_{BR}(z)$  are derived from the left and right probability density functions ( $\Phi_L(C(x < x_{max}/2, z))$ )  
 238 and ( $\Phi_R(C(x > x_{max}/2, z))$ ), respectively, for each flight transect level. Specifically, for  $\Phi_L$  and  $\Phi_R$ , Gaussian  
 239 functions are fit to the distributions for the plume distribution ( $\Phi_P$ ) and the background distribution ( $\Phi_B$ ).  
 240 In practice,  $\Phi_B$  is well described by a single Gaussian, while  $\Phi_P$  is best described by multiple Gaussian  
 241 functions. Then,  $C_{BL}(z)$  and  $C_{BR}(z)$  are defined such that,

$$242 \int \Phi_{BL}(C_{BL}(z)) = 0 \text{ and } \int \Phi_{BR}(C_{BR}(z)) = 0. \quad (1)$$

243 where  $\Phi_{BL}$  and  $\Phi_{BR}$  are the background  $\Phi_B$  for the left and right halves of the data plane, respectively.  
 244 Concentration is not a conserved value, thus  $C$  is converted into mass ( $N'$ ) by the ideal gas law for spatial  
 245 integration to derive the total emissions ( $E$ ), which is the integration of the flux through the plane,  $Q$ ,

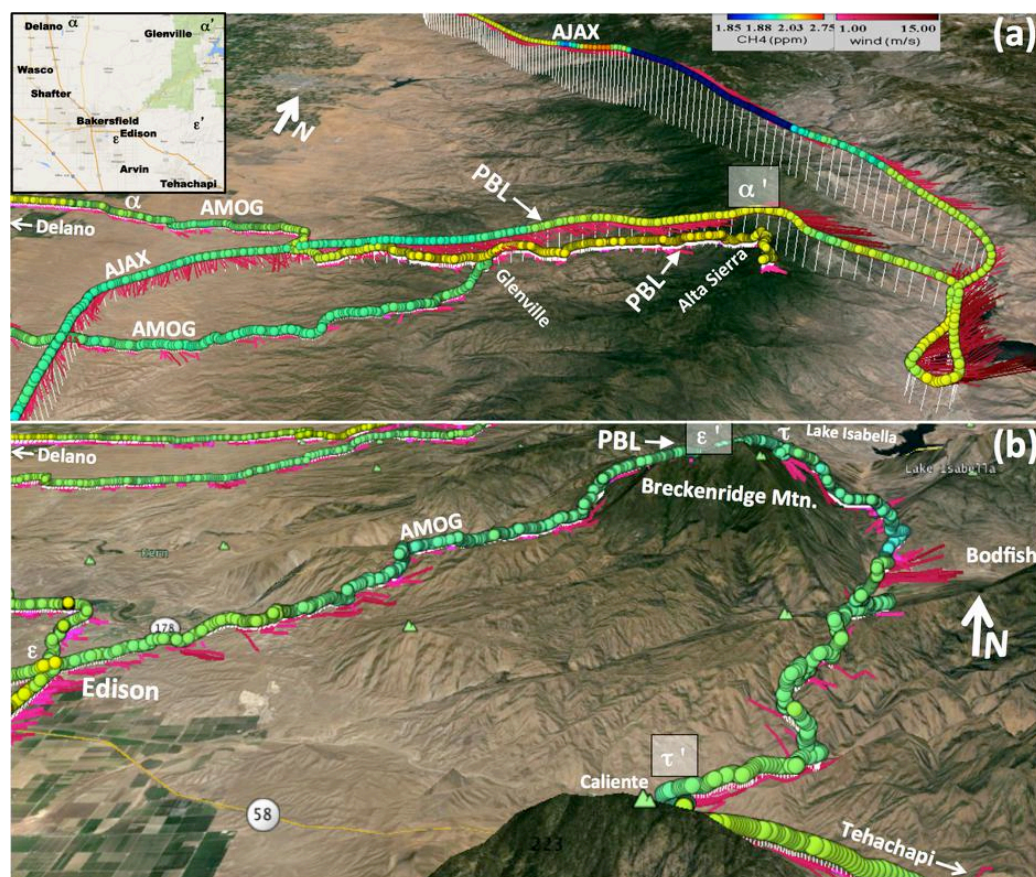
$$246 E = \int_{x_1}^{x_2} \int_0^{z=PBL} Q(x, z) dz dx \quad (2)$$

## 247 2.5. Uncertainty evaluation for emission calculation

248 A flux estimate requires two types of assumptions with respect to the flux calculation: representativeness  
 249 and appropriateness. Specifically, background concentration profiles may be incorrect, while winds,  
 250 which are measured accurately, could be un-representative, as could concentrations due to temporal  
 251 variability over the period needed to make the measurements. Monte Carlo simulations based on observed  
 252 data variability were run to assess uncertainty. Instrumental uncertainty is far less than spatial and  
 253 temporal variability and hence appropriateness is the dominant source of uncertainty.

254

255 Monte Carlo simulations were based on 1 standard deviation in  $U_N(z)$  around the mean for each flight  
 256 transect altitude level. Gaussian distributions were created with half widths of 4 seconds and randomly  
 257 sampled to populate  $U_N(x, z)$ , which then was interpolated vertically for the flux calculation. Other  
 258 variables were allowed to vary in a similar manner and sampled by the Monte Carlo simulations. Monte  
 259 Carlo simulations addressed uncertainties in  $C_B(z)$  based on the data variability at the edges of the data  
 260 plane. This addresses uncertainty in precisely from where the inflowing air is arriving, which alters the  
 261 background concentration in the flux calculation. One million Monte Carlo simulations were run for a  
 262 flux uncertainty calculation.



263  
264 **Figure 3.** (a) Pre-survey, upwind AMOG surface and AJAX airborne methane ( $\text{CH}_4$ ) and winds for  
265 vertical profile on the Delano – Alta Sierra transect ( $\alpha$ – $\alpha'$ ). Inset shows area map. (b) Post survey,  
266 downwind AMOG surface profile ascent Edison-Breckenridge ( $\epsilon$ – $\epsilon'$ ) and descent Breckenridge-Bodfish-  
267 Caliente ( $\tau$ – $\tau'$ ). Upwind profile visible top left. Planetary boundary layer (PBL) identified.

### 268 3. Results

#### 269 3.1. Profile data

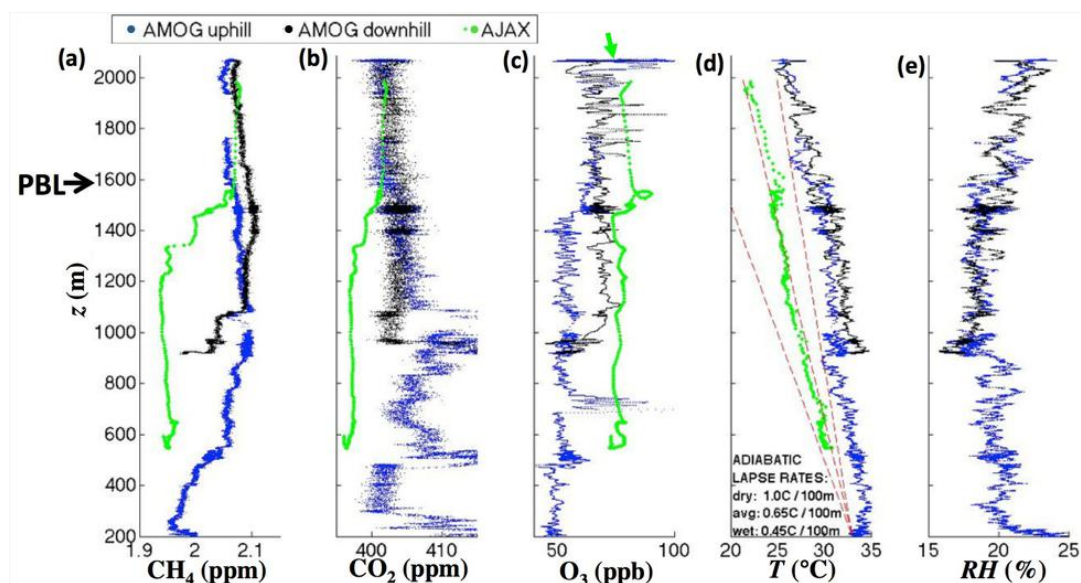
270 Four vertical profiles (surface and airborne) were collected to understand PBL evolution during the  
271 survey (2 hrs.) and across the survey domain. AMOG and AJAX collected pre-survey intercomparison  
272 vertical profiles ~30 km north of the Kern Fields between the small town of Delano on the SJV floor (100  
273 m) up to Shirley Meadows (2100 m) on a ridge of the Greenhorn Mountains in the Sierra Nevada  
274 Mountain Range (Fig. 3). This profile spans a wide range of topography, from grasslands on rolling hills,  
10



275 to tall pine trees near Alta Sierra, see Supp. Fig. S5 for surface images along the profile. AMOG also  
276 conducted a post-survey, downwind vertical atmospheric profile to 1800 m. Approximately 15 minutes of  
277 data were collected in an open (200–300 m) field above Shirley Meadows (2258 m) that was fairly  
278 exposed with only thin stands of pine trees on terrain falling steeply off to both sides.

279

280 The AMOG vertical ascent was collected before the AJAX profile to enable concurrent AMOG/AJAX  
281 data collection for the Kern Fields. The AMOG ascent/descent was from 18:48 to 21:09 (20:08 UTZ at  
282 crest), while AJAX flew a descent pattern from 20:58 to 21:04 UTC. The AMOG descent was shortened  
283 to ~1000 m altitude (Glenville, CA) to allow AMOG to reach the Kern Fields nearly concurrent with  
284 AJAX and GOSAT.



285

286 **Figure 4.** Surface altitude ( $z$ ) profiles for west-east Delano-Alta Sierra transect (Fig. 3A,  $\alpha$ - $\alpha'$ ) for  
287 AMOG and AJAX (a) methane ( $\text{CH}_4$ ), (b) carbon dioxide ( $\text{CO}_2$ ), (c) ozone ( $\text{O}_3$ ), (d) temperature ( $T$ ), and  
288 (e) relative humidity ( $RH$ ). Also shown on (d) are the dry, average, and wet adiabatic lapse rates. Data key  
289 on panel, planetary boundary layer (PBL), labeled. Green arrow shows extrapolation of AJAX trend to  
290 Shirley Meadows altitude (2258 m).

291 Overlapping AMOG and AJAX profile data were collected between 500 and 2000 m. There was very  
292 good agreement between the two platforms for  $\text{CO}_2$  and  $\text{CH}_4$  for altitudes between 1.55 and 2 km (Fig. 4a  
293 and 4b). AMOG and AJAX  $\text{CH}_4$  concentrations decreased notably from the well-mixed PBL to the near  
294 surface layer, from ~2.07 ppm (500-750 m) to ~1.93 ppm (250-300 m). AJAX also showed a decrease in  
295  $\text{CO}_2$  from 403 ppm to below 400 ppm. The  $\text{CO}_2$  decrease was consistent with a shift to agricultural air  
11



296 where CO<sub>2</sub> vegetative uptake reduces CO<sub>2</sub> concentrations. The PBL grew from 600 to 900 m between  
297 AMOG's ascent and descent and then to 1500 m by the time of AJAX's descent based on the CH<sub>4</sub>, CO<sub>2</sub>,  
298 and O<sub>3</sub> data.

299

300 The PBL was identified at ~1580-1600 m based on both surface and airborne relative humidity (*RH*) and  
301 temperature (*T*) vertical profiles. Diurnal heating is apparent between the two AMOG Surveyor *T* profiles,  
302 but does not change the lapse rate. Because AJAX flies above the surface where AMOG collects data,  
303 AJAX temperatures are lower. In the lower atmosphere, the lapse rate was 6.9°C km<sup>-1</sup> for AJAX between  
304 500-900 m, while the AMOG lapse rate from 200-900 m was a similar 5.6°C km<sup>-1</sup>. Between 950 and the  
305 top of the PBL, AMOG lapse rates were much shallower, 2.5 °C km<sup>-1</sup>, with a jump in temperature at 900  
306 m. Above the PBL, the AMOG lapse rate was 3.5°C km<sup>-1</sup>, close to the wet adiabatic lapse rate (Fig. 4d).

307

308 Above the PBL, O<sub>3</sub> concentrations between AMOG and AJAX were ~20 ppb different although the  
309 AMOG and AJAX profile slope (dO<sub>3</sub>/dz) were the same. If the trend in AJAX O<sub>3</sub>(*z*) from 1600 to 1850 m  
310 is extended to *z* = 2258 m (Fig. 3C, green arrow), there is agreement with AMOG Shirley Meadows (open  
311 field) O<sub>3</sub> concentrations. This similar slope but different absolute value could indicate O<sub>3</sub> loss as it  
312 diffused down through the pine canopy to the surface (and AMOG). Tall pine trees dominate above  
313 ~1700, except for Shirley Meadows where, as noted, there was agreement. This difference does not arise  
314 from calibration differences; the AMOG Surveyor O<sub>3</sub> analyzer was cross calibrated with the AJAX  
315 calibration source. For 900 < *z* < 1400 m, AJAX - AMOG agreement was better for the descent, which  
316 was closer in time to AJAX than the ascent. This shift likely was associated with formation of the daytime  
317 PBL.

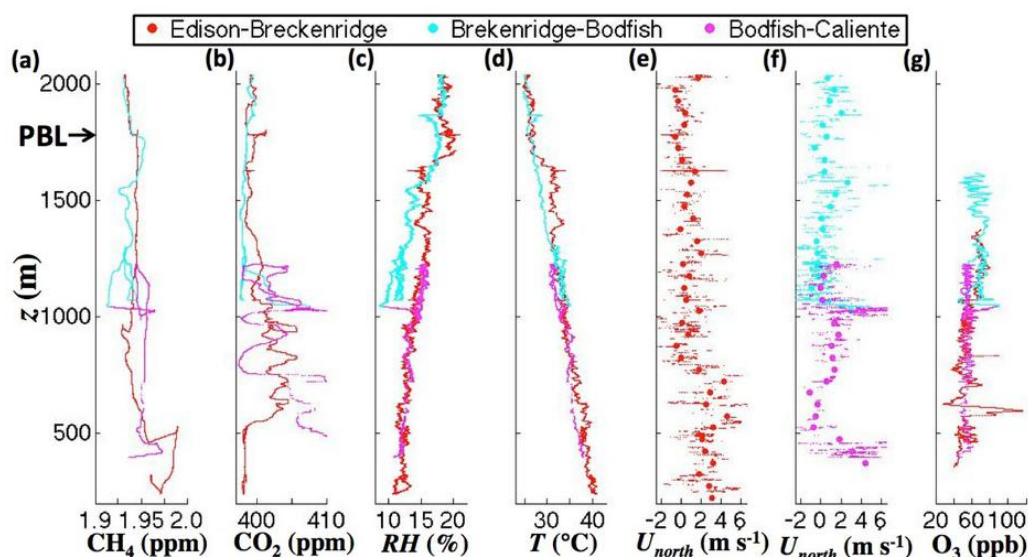
318

319 AJAX observed elevated O<sub>3</sub> that was well mixed down to 500 m, while earlier AMOG showed well-  
320 mixed O<sub>3</sub> down to only 1100 m. There also was a small (~10 ppb) O<sub>3</sub> enhancement at the top of the PBL  
321 in both the airborne and surface profiles. The highest O<sub>3</sub> concentrations were observed by AMOG in  
322 Shirley Meadows, where visibility was low due to smoke aerosols from the Rough Fire (NASA, 2015).  
323 Air above the PBL was more humid than elsewhere in the profile, except for the lowest 50 m above the  
324 valley floor, which was enriched in CH<sub>4</sub>, CO<sub>2</sub>, and *RH*, possibly from nocturnal accumulation and  
325 agriculture including irrigation *RH* inputs. There were thin, atmospheric layers that suggest remnant  
326 structures from the prior day. For example at ~550 m the air changed character, with a jump in CO<sub>2</sub> by  
327 ~10 ppm, and of O<sub>3</sub> by ~ 10 ppb, and a decrease in the CH<sub>4</sub> altitude gradient (dCH<sub>4</sub>/dz).

328



329 Air was more polluted at greater altitude above the PBL in the upwind (Delano – Alta Sierra) profile for  
 330 O<sub>3</sub> for both platforms with air 10-20 ppb greater than in the PBL. Additionally, AJAX CH<sub>4</sub> and CO<sub>2</sub> were  
 331 significantly higher above the PBL. The AMOG CH<sub>4</sub> and CO<sub>2</sub> data are less clear, presumably because  
 332 AMOG data were prior to the disappearance of the nocturnal, stably stratified PBL. This was consistent  
 333 with visual observations of haze by AMOG from Shirley Meadows as well as by the AJAX pilot. Also,  
 334 air above the PBL was more humid.

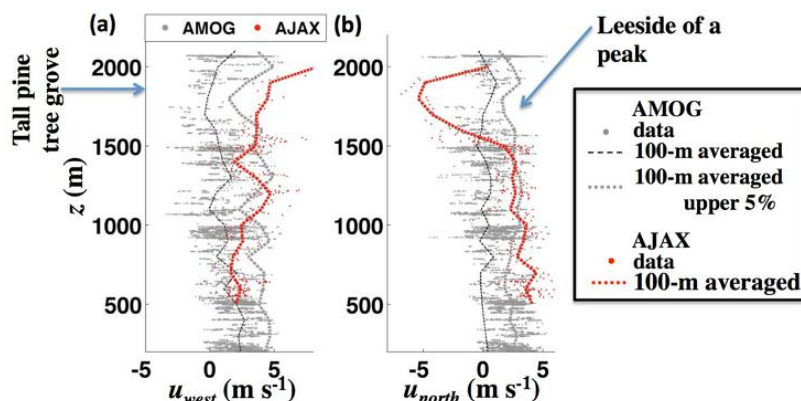


335  
 336 **Figure 5.** Surface altitude ( $z$ ) profiles for Edison-Breckenridge ascent (red) and descent (blue) to Bodfish  
 337 and then Caliente profile (magenta) (Fig. 3b) for AMOG Surveyor (a) methane (CH<sub>4</sub>), (b) carbon dioxide  
 338 (CO<sub>2</sub>), (c) relative humidity ( $RH$ ), (d) temperature ( $T$ ), north wind ( $U_{north}$ ), for (e) ascent and (f) descent,  
 339 and (g) ozone (O<sub>3</sub>). Planetary Boundary Layer (PBL) labeled.

340 A downwind ascent profile in the SJV was collected from Edison, CA to the high flanks of Breckenridge  
 341 Mountain, followed by a descent behind the Breckenridge Mountain to Caliente, CA through the tiny  
 342 town of Bodfish (Fig. 3b). This descent was separated from the SJV by a ridge and includes dryer, clean  
 343 air is that is representative of air from around Lake Isabella, a fairly isolated mountain valley. The  
 344 downwind profile was collected quasi-Lagrangian in that the time separating the two profiles (about four  
 345 hours) is comparable to the transport time (75 km at 4 m s<sup>-1</sup>, implies 5 hours for transport). Thus, the  
 346 downwind profile was for close to the same air. Over these hours, there was some additional PBL  
 347 development, ~100 m to ~1675 m, with highly uniform CH<sub>4</sub> between 1000 m and the top of the PBL (**Fig.**  
 348 **5a**). Thus, the PBL remained fairly stable over the course of the study. Air in both the upper PBL and



349 above was cleaner with lower humidity and CH<sub>4</sub> concentrations. Unfortunately, the O<sub>3</sub> analyzer  
350 overheated during the ascent and resumed collecting data on the descent at ~1500 m.



351

352 **Figure 6.** Altitude ( $z$ ) profiles for (a) west (upslope) and (b) north (cross slope) wind components from  
353 AMOG and AJAX for overlapping altitudes of the Delano–Alta Sierra transit (Fig. 3,  $\alpha$ – $\alpha'$ ), 100-m  
354 altitude rolling-averaged data for AJAX, AMOG, and AMOG upper 5% of winds. Data key on figure.

355 Direct comparison between AMOG and AJAX winds is inappropriate because AMOG winds are affected  
356 strongly by obstacles including hills, trees, and buildings. However, in many instances, terrain is open, or  
357 gently rolling hills, and there tend to be regions of stronger winds that we propose are representative of  
358 free atmosphere winds. AMOG data were altitude binned and the strongest winds in each bin were  
359 compared with AJAX (Fig. 6). Agreement is generally good (within 15-20%) between the upper 5% of  
360 AMOG cross-slope (west) winds in each altitude-averaged band (Fig. 6a). For the upslope wind (north)  
361 agreement is better (within 5-10%) for a larger range of altitudes (Fig. 6b). This allows fusions of the  
362 upper 5% of AMOG winds with AJAX winds.

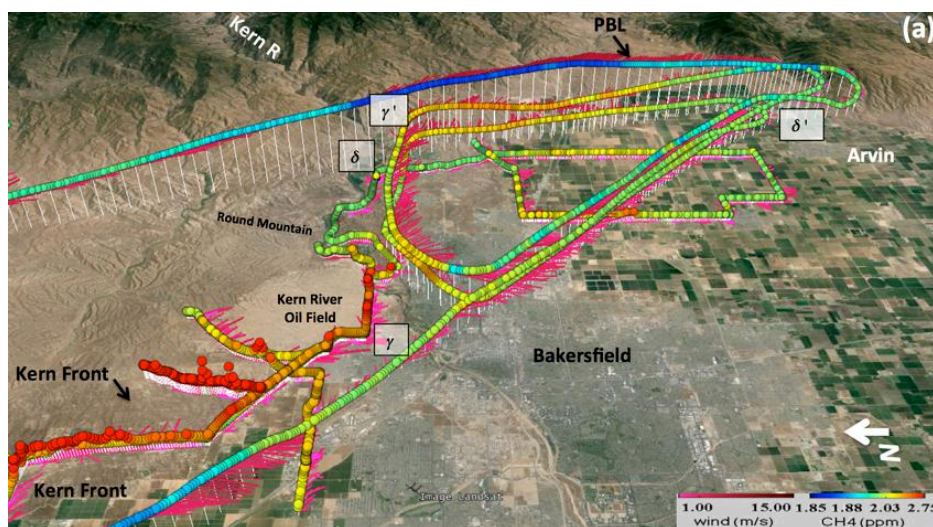
### 363 3.2. Kern Fields and Bakersfield Greenhouse Gas Emissions

#### 364 3.2.1 Methane

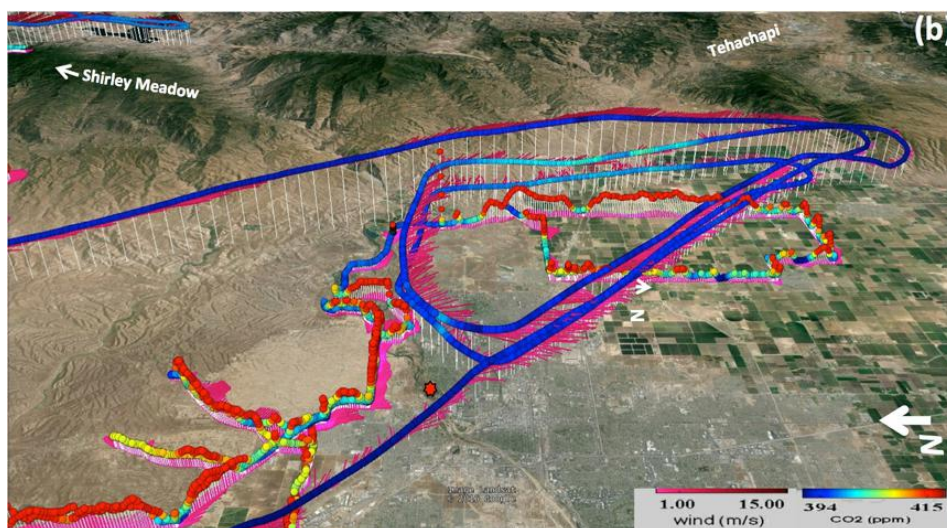
365 On 19 Aug. 2015, winds over the Kern Fields were prevailing (northwesterly) and fairly strong ( $\sim 3 \text{ m s}^{-1}$ )  
366 on the ground and somewhat stronger aloft (Fig. 7). As a result, surface topography like the Kern River  
367 Bluffs imposed only small wind modification at the surface and at altitude. Southeast of Bakersfield,  
368 winds veered to westerly's towards passes in the Sierra Nevada Mountains that connect to the Mojave  
369 Desert. The downwind survey included two plume transits on agricultural roads with negligible to no  
370 traffic. These transits clearly showed the plume's eastward drift, passing to the north of the small town of  
371 Arvin, CA.



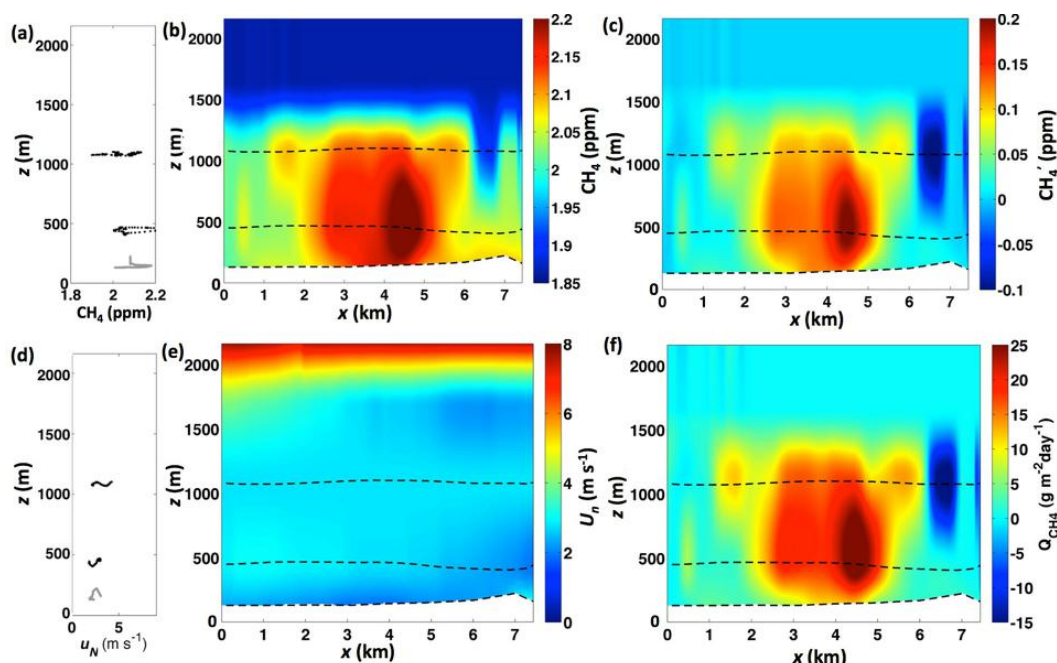
372



373



374 **Figure 7.** Combined AJAX and AMOG winds and *in situ* (a) methane (CH<sub>4</sub>) and (b) carbon dioxide  
 375 (CO<sub>2</sub>) for the Kern Fields on 19 Aug. 2015 for prevailing wind conditions. Greek letters identify two  
 376 downwind curtains. Red star on (b) locates origin for transect  $\gamma$ - $\gamma'$ . Data keys on figure.



377

378 **Figure 8.** (a) Methane (CH<sub>4</sub>) altitude ( $z$ ) profiles for 19 Aug. 2015 for AJAX (black) and AMOG (gray)  
 379 data. (b) Interpolated, fused AJAX and AMOG CH<sub>4</sub> data, with respect to lateral east distance ( $x$ ) relative  
 380 to 119.0023°W, 35.3842°N for data plane  $\gamma$ - $\gamma'$  (Fig. 7). Dashed lines show data locations. (c) CH<sub>4</sub>  
 381 anomaly (CH<sub>4</sub>') relative to the background data plane (Supp. Fig. S6A). (d) Vertical normal wind profile  
 382 ( $U_n$ ) from AJAX (black) and AMOG (gray) data during ascent/descent, (e) interpolated, fused  $U_n$ , and (f)  
 383 CH<sub>4</sub> flux ( $Q_{CH_4}$ ) for the Kern Fields. Data key on panels.

384 The background CH<sub>4</sub> plane  $C_B(x,z)$  was extracted from the CH<sub>4</sub> data outside the plume –  $C_{BL}(z)$  and  
 385  $C_{BR}(z)$ , see Eqn. (1) – immediately downwind of the Kern Fields (transect  $\gamma$ - $\gamma'$ ).  $C_B$  showed a slight  
 386 increase towards the east of ~20 ppb (Supp. Fig. S6a). Emissions from the Kern Fields' were dominated  
 387 by a large, focused CH<sub>4</sub> plume (or group of plumes) in the core of a much broader, dispersed, and poorly  
 388 defined plume. This structure is evident in both surface AMOG data and in the lowest AJAX altitude for  
 389 plane  $\gamma$ - $\gamma'$  with both showing the strongest peak at  $x = 4.5$  km (Fig. 8b, dashed lines). Within the plume,  
 390 concentrations are elevated at altitude relative to the surface, indicating buoyant rise. The upper AJAX  
 391 flight line was several hundred meters below the top of the PBL (at ~1580 m, Fig. 4) and constrains the  
 392 main plume, which was centered in the PBL. Concentrations above the PBL were determined from AJAX  
 393 descent and ascent data (Fig. 4), which agreed with AMOG observations above the PBL. These  
 394 observations show that the plume was not well mixed across the PBL. Two other small plumes were  
 395 observed at  $x \sim 1.7$  and 5.7 km that were not mirrored in surface data and were centered at the top of the  
 16





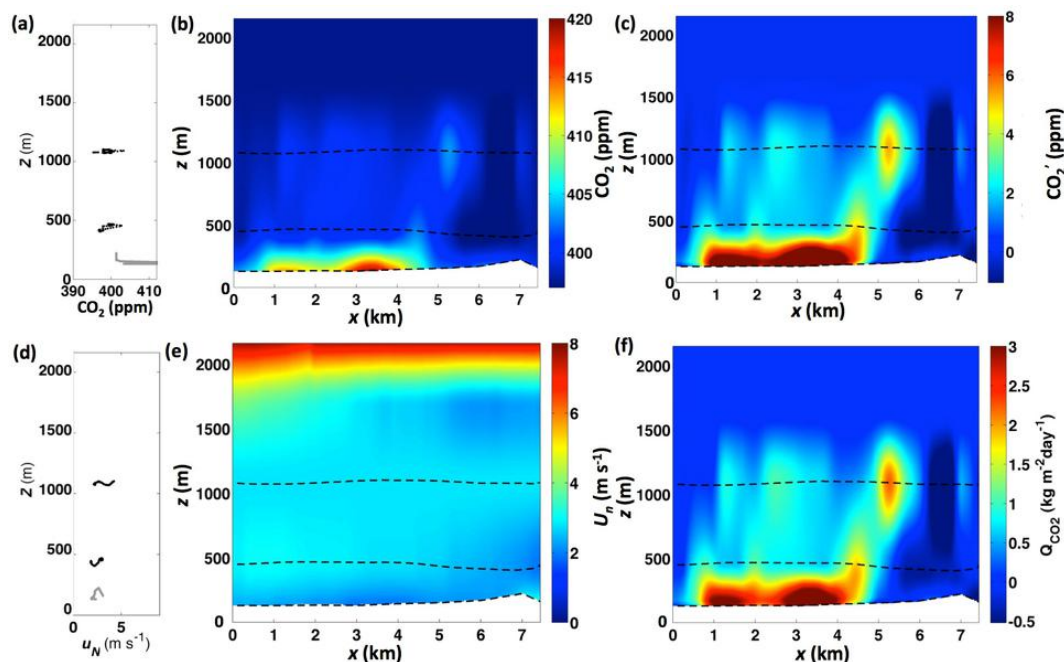
396 PBL, indicating strong buoyant rise within the PBL. The upper altitude clean air intrusion at  $x \sim 6.5$  km lies  
397 downwind of Round Mountain Canyon to the east of the Kern River oil field (Fig. 8b, Fig. 7a for  
398 location), but did not penetrate down to 500 m. The normal wind ( $U_n$ ) was fairly uniform across the data  
399 plane, including downwind of the canyon (Fig. 8e). Thus, the  $\text{CH}_4$  flux ( $Q_{\text{CH}_4}(x, z)$ ) shows similar spatial  
400 patterns to  $\text{CH}_4'(x, z)$ . Total estimated emissions ( $E$ ) were  $32 \pm 16$  Gg  $\text{yr}^{-1}$ .

401

402 For comparison, a recent bottom-up estimate of  $\text{CH}_4$  emissions based on production data for the Kern  
403 Fields estimated 10-40 Gg  $\text{CH}_4$   $\text{yr}^{-1}$  (68% Confidence Level), by combining oil and gas production data  
404 with US-EPA emissions factors for associated wells (Jeong et al., 2014). Other  $\text{CH}_4$  sources are unlikely  
405 to confuse this interpretation as petroleum system emissions are  $\sim 20$  times larger than estimated nearby  
406 livestock and landfill  $\text{CH}_4$  emissions of  $\sim 2.3$  and 1.4 Gg  $\text{yr}^{-1}$ , respectively (Calgem, 2014).

### 407 3.2.2. Carbon Dioxide

408 Background  $\text{CO}_2$  for data curtain  $\gamma - \gamma'$  (Supp. Fig. S6b) was highly uniform. Given the strong crosswinds  
409 and care taken to avoid trailing other vehicles on the low-trafficked China Loop Road, these data passed  
410 quality review— $\text{CO}_2$  exhaust contamination manifests as a dramatic increase in the standard deviation as  
411 AMOG intersects a turbulent vehicle exhaust plume. There was a shallow  $\text{CO}_2$  layer constrained to the  
412 lower 100 to 200 m with  $\sim 10$  ppm enhancement (Fig. 9a), also observed in the  $\text{CO}_2$  vertical profile (Fig.  
413 4b), a layer that was characterized by elevated relative humidity. Further evidence that these broad spatial  
414  $\text{CO}_2$  emissions are real is from the spatial similarity to  $\text{CO}_2$  enhancements in the lowest AJAX flight data  
415 (Fig. 9c). For example the surface  $\text{CO}_2$  plume was strongest at  $x \sim 4.5$  km in AMOG and AJAX data. The  
416 broad spatial extent of these emissions, similar to the broad  $\text{CH}_4$  emissions suggests a relationship to  
417 field-scale (engineering or geological) processes. Overall  $\text{CO}_2$  emissions were  $2.4 \pm 1.2$  Tg  $\text{yr}^{-1}$ .



418

419 **Figure 9.** (a) Vertical carbon dioxide ( $\text{CO}_2$ ) altitude ( $z$ ) profile data for 19 Aug. 2015 for AJAX (black)  
 420 and AMOG (gray) data. (b) Interpolated, fused AJAX and AMOG  $\text{CO}_2$  data curtain with respect to lateral  
 421 east distance,  $x$ , relative to  $119.0023^\circ\text{W}$ ,  $35.3842^\circ\text{N}$  for curtain  $\gamma-\gamma'$  (Fig. 7b). Dashed lines show data  
 422 locations. (c)  $\text{CO}_2$  anomaly ( $\text{CO}_2'$ ). (e) Vertical normal wind profile ( $U_n$ ). (e) Interpolated, fused  $U_n$ , and  
 423 (f)  $\text{CO}_2$  flux ( $Q_{\text{CO}_2}$ ) for the Kern River and Kern Front oil fields for 19 Aug. 2015. Data key on panels.

424 There was a strong  $\text{CO}_2$  anomaly in a focused plume at  $x = 5$  km and  $z = 1$  km. This plume likely relates  
 425 to the two cogeneration power plants located in the Kern River oil field. Further support for this  
 426 interpretation is its co-location with a similarly focused  $\text{CH}_4$  plume at the same location. This power  
 427 plant-related feature is a persistent feature that has been observed in other surveys (Leifer – unpublished  
 428 data). The upper clean air intrusion in the  $\text{CH}_4$  data curtain also is apparent in the  $\text{CO}_2$  data (Fig. 9b), in  
 429 front of Round Mountain Canyon (Fig. 7).

430

431 Based on a reservoir  $\text{CO}_2:\text{CH}_4$  gas ratio of 92.2%:1.7% (Lillis et al., 2008) and  $32 \text{ Gg yr}^{-1}$   $\text{CH}_4$  emissions,  
 432 the Kern Fields'  $\text{CO}_2$  emissions were predicted to be  $1.8 \text{ Tg yr}^{-1}$ , which is fairly consistent with the  
 433 directly derived emissions of  $2.4 \text{ Tg yr}^{-1}$ . Both these values are somewhat lower than the inventory for the  
 434 cogeneration plants in Kern River oil field -  $3.1 \text{ Tg yr}^{-1}$  (CARB, 2016). The disagreement with inventory  
 435 likely arises from intermittent activity, which was observed during the GOSAT-COMEX campaign.

436



#### 437 4. Discussion

##### 438 4.1. Experimental design and real-time visualization

439 Ideally, GCE airborne and surface data are collected first upwind and then downwind. However, AJAX  
440 airborne data are not collected Lagrangian as would be necessary for slower, less maneuverable airborne  
441 platform thanks to its extreme speed and maneuverability. This allows collection of near snapshot (~30  
442 minutes) data. Slower, AMOG surface data were collected quasi-Lagrangian, reducing the likelihood of  
443 confounding interference in the study area from non-FFI SJV inputs due to wind shifts after the pre-  
444 survey (for non-nominal winds the collection is aborted). Given the AJAX-AMOG speed difference,  
445 concurrent surface and airborne data could not be collected both upwind and downwind, and thus,  
446 concurrency was prioritized for downwind. For flight efficiency and to provide downwind concurrency  
447 with AMOG, AJAX flew a triangle that allowed AJAX to complete transects at three altitudes in close to  
448 AMOG's upwind-downwind survey time.

449

450 After the Kern Fields survey, AJAX returned to base, while AMOG collected additional surface data,  
451 exploring the fate of emissions from the Kern Fields. The word, “exploring” is significant, as real-time  
452 visualization of winds, CH<sub>4</sub>, and O<sub>3</sub> guided the downwind surveying. Data were collected to test the  
453 hypothesis that there was a relationship between wind strength and the specific outflow path from the SJV  
454 to Mojave Desert - specifically, that more northerly passes, which require greater wind veering from  
455 prevailing are preferred at lower winds speeds. The AMOG survey first confirmed that outflow was not  
456 up the Kern River Valley, and then collected a downwind vertical profile into the Sierra Nevada  
457 Mountains to search for outflow through a pass near Breckenridge Mountain. After confirming its  
458 absence, AMOG then investigated in the Tehachapi Pass, where the outflow was identified. Thus, on 19  
459 Aug. 2015, when winds were strong, the outflow was by the most direct pathway - the Tehachapi Pass.

##### 460 4.2. Experimental design and uncertainty reduction

461 The experimental design reduced uncertainty by better characterizing the PBL through surface and  
462 airborne data fusion so that a well-mixed PBL is not required. Airborne data characterizes CH<sub>4</sub> and winds  
463 in the PBL and above, while surface data characterizes the atmosphere below where airplanes are  
464 permitted to fly due to airspace restrictions, e.g., cities, approach pathways, military airspace, and/or  
465 safety. The *in situ* analyzers record concentration and winds with very high accuracy; however, only at a  
466 single location and time. Thus, *in situ* uncertainty arises mostly from inadequate characterization of  
467 temporal variability and spatial heterogeneity.



468

469 Aerial survey altitudes were designed to span from near the top of the PBL to as low as permissible and  
470 an intermediate level (0.5, 1, 1.2 km). Thus, surface data added information on the lowest third of the  
471 1.58-km thick PBL. This lower portion of the PBL is more important on days when the PBL is shallower.

472

473 For a well-mixed PBL, surface - airborne data fusion does not reduce uncertainty; however, these  
474 observations showed that the well-mixed PBL assumption often may be poor (even 10-20 km downwind).  
475 One solution is to collect data even further downwind, where the PBL is more well-mixed (White et al.,  
476 1976); however, secondary (potentially uncharacterized) sources downwind of the study area and upwind  
477 of the downwind data plane add confounding anomalies. Also, wind flow complexity can lead to transport  
478 orthogonal to the overall downwind direction, leading to flux leakage out of the plume. The likelihood of  
479 plume loss increases over greater distances. And finally, as the PBL evolves with time, it imposes an  
480 evolving structure on the wind and concentration vertical profiles, which also challenge the well-mixed  
481 PBL assumption – particularly if transport to the downwind plane requires hours.

482

483 Uncertainty also arises from wind and emission variability over the survey time period. The best strategy  
484 is to minimize study time; however, there is a necessary tradeoff between spatial resolution and study  
485 time. AJAX collects data quickly, allowing survey completion within far less than typical atmospheric  
486 change timescales. Similarly, the surface survey route was designed to minimize collection time,  
487 primarily on rural/agricultural roads carefully selected to avoid traffic congestion and traffic lights. The  
488 surface survey requires ~90 minutes to complete and is conducted quasi-Lagrangian.

489

490 GCE treats uncertainty explicitly, allowing improvements in the data collection strategy to reduce  
491 uncertainty. For example, the east-west downwind transect was lengthened from earlier data collects to  
492 characterize background concentrations better. GCE also does not require an *a priori* emission  
493 distribution and thus incorporates explicitly emissions from super-emitters, normal emitters, and  
494 distributed sources, improving robustness of the findings. In contrast, inversion models require a  
495 reasonable spatial *a priori* emission distribution and the ability to model transport across the study  
496 domain. However, complex wind flows from fine-scale topographic structures, as observed for the Kern  
497 Fields, challenge transport modeling.

#### 498 **4.3. Profile intercomparison**

499 Above the PBL, there was excellent agreement between surface and airborne concentration profile data,  
500 while concentration profiles within the PBL show significant differences between the two profiles, likely  
20



501 related to air mass shifts and diurnal heating during the time between the profiles (Fig. 4). Winds above  
502 the PBL were in poor agreement, with the north component in the opposite direction (Fig. 6). Underlying  
503 this discrepancy was a mountain peak, which clearly caused large-scale alterations in the wind flow field.

504

505 Within the PBL, agreement between unfiltered surface AMOG winds and AJAX winds was poor,  
506 unsurprising because surface winds are strongly affected by obstacles. However, by filtering AMOG  
507 winds (collected 3-m above the surface) for the strongest 5%, agreement was within 15-20% for the  
508 along-slope – i.e., north – winds, and better for upslope winds (west). Specific exceptions were when  
509 AMOG was in a dense grove of pines, and when AJAX flew behind into the lee of a mountain peak.  
510 Surface winds are modulated by a wide range of surface factors including trees, steep hills and hillocks,  
511 blocking by a steep slope, rolling hills, and structures (Supp. Fig S5). However, a combination of gusts  
512 (among thin wooded terrain on steep slopes) and the limited spatial extent of most obstacles underlies the  
513 agreement between the filtered AMOG and AJAX wind profiles. Agreement is better for the upper  
514 portions of the PBL (within 10-20%) where Sierra Nevada Mountain slopes are steeper. In contrast, the  
515 slope lower in the PBL is gentle, and surface boundary layer effects are more pronounced, biasing wind  
516 speeds slower.

517

518 The wind orientation to the slope affects the comparison because topography imposes wind field structure  
519 at large and small scales. Where winds advect air upslope, transport incorporates a non-negligible vertical  
520 component that is missed by the 2D sonic anemometer used in the study reported here. The current  
521 AMOG configuration measures 3D winds, as does AJAX.

522

523 Some of the discrepancy between AMOG and AJAX wind profiles could have arisen from temporal  
524 changes between the two profiles; however, this is unlikely for two reasons. First, the top of the PBL was  
525 identified four times over the course of the study and remained stable within 100 m across the domain.  
526 And second, surface wind observations remained relatively constant after the mid-morning shift to  
527 daytime conditions (breakup of nocturnal stratification). However, the poor agreement between AJAX  
528 and AMOG vertical concentration profiles within the PBL suggests significant air mass shifts –  
529 highlighting the need for better concurrence.

#### 530 **4.4. GHG FFI emissions**

531 Emissions for the Kern Fields were estimated at  $32 \pm 16$  Gg  $\text{CH}_4$   $\text{yr}^{-1}$  with  $\text{CH}_4$  emissions ~20% above  
532 EPA inventories, and  $2.4 \pm 1.2$  Tg  $\text{CO}_2$   $\text{yr}^{-1}$ . The broad  $\text{CO}_2$  plume suggests emissions from the geologic  
533 reservoir – likely along the same pathways associated with  $\text{CH}_4$  leakage – in addition to the focused  
21



534 emissions from the co-generation power plants. On China Loop Road (where the CO<sub>2</sub> surface plume was  
535 transected), strong crosswinds and light traffic would have prevented significant vehicular CO<sub>2</sub>  
536 contamination.

537

538 For comparison, a recent bottom-up estimate of CH<sub>4</sub> emissions from the Kern Fields estimated 25±15 Gg  
539 CH<sub>4</sub> yr<sup>-1</sup> by combining oil and gas production data with emissions factors for associated wells used by  
540 US-EPA (Jeong et al., 2014). Thus, 19 Aug. 2015 CH<sub>4</sub> emissions were a third above inventories. A  
541 number of factors likely play a role including the age of the Kern River oil field (over a century),  
542 production factors (steam injection), shallowness of the reservoir (<300 m), location in a tectonically  
543 active area, which creates alternate migration pathways from the reservoir (Leifer et al., 2013), and the  
544 recent expansion of the number of wells in the Kern Front oil field (from GoogleEarth timeline imagery).  
545 Many of these factors are common to other production fields in California, the US, and globally.

546

547 These results agree with a recent metastudy of field studies of FFI production emissions, which showed  
548 significant underestimation in the EPA budget (Brandt et al., 2014; Miller et al., 2013). Given the  
549 importance or dominance of FFI emissions in anthropogenic greenhouse gas budgets, an increase of 25-  
550 50% of the FFI contribution requires either reduction in another budget category, and/or an increase in the  
551 loss rate. However, a recent husbandry emissions study also suggested significant underestimation  
552 (Gentner et al., 2014). Thus, the present study supports the hypothesis that CH<sub>4</sub> loss rates are  
553 underestimated. For example a recent study identified a new loss mechanism in near-surface soils  
554 (Fernandez-Cortes et al., 2015). In any case, this study highlights the need for improved measurement  
555 tools to reduce the significant uncertainty in the CH<sub>4</sub> budget and also satellite measurement validation,  
556 particularly for complex terrain and in the source's near field. Mountainous terrain affects about half the  
557 earth's population and half the earth's surface (Meyers and Steenburgh, 2013).

## 558 5. Conclusion

559 This study showed how to combine airborne and surface *in situ* data to improve emissions derivation, and  
560 demonstrated the novel use of topography to characterize vertical atmospheric structure with a surface  
561 mobile platform. Given that mountains cover a significant fraction of the earth's land surface, and that  
562 airplane logistics often are beyond the available resources for many researchers, there are many  
563 opportunities to apply these techniques globally. Data showed the PBL was not well-mixed, even 10-20  
564 km downwind, highlighting the importance of the direct flux quantification experimental design.

565

566 **Table of Nomenclature**

567		Units	Description
568	AJAX	(-)	Alpha Jet Atmospheric eXperiment
569	AMOG	(-)	AutoMOBILE trace Gas
570	Bbl	(-)	Barrel (of oil) 1 bbl = 6.38 m <sup>3</sup>
571	COMEX	(-)	CO <sub>2</sub> and MEthane eXperiment
572	EOR	(-)	Enhanced oil recovery (techniques)
573	EPA	(-)	Environmental Protection Agency
574	GCE	(-)	GOSAT COMEX Experiment
575	GHG	(-)	Greenhouse Gases
576	GOSAT	(-)	Greenhouse gases Observing SATellite
577	GHG	(-)	Greenhouse gas
578	PBL	(-)	Planetary Boundary Layer
579	SJV	(-)	San Joaquin Valley
580	Tg		Terragram (10 <sup>12</sup> g)
581	UTZ	(-)	Universal time
582	$C'(x,z)$	(ppm)	concentration anomaly (above $C_B$ )
583	$C(x,z)$	(ppm)	concentration
584	$C_B(x,z)$	(ppm)	background concentration – outside plume
585	$C_{BL}(z)$	(ppm)	background concentration profile – left side of profile
586	$C_{BR}(z)$	(ppm)	background concentration profile – right side of profile
587	$E$	(mol s <sup>-1</sup> )	Emission source strength
588	$N'$	(mol cm <sup>-3</sup> )	molar mass anomaly
589	$Q(x,z)$	(mol m <sup>-2</sup> s <sup>-1</sup> )	Flux through the data plane
590	$R^2$	(-)	Correlation coefficient
591	$RH$	(%)	Relative humidity
592	$T$	(°C)	Temperature
593	$U_n(x,z)$	(m s <sup>-1</sup> )	Winds normal to the data plane, a function of (x, z)
594	$U_{north}$	(m s <sup>-1</sup> )	North wind component
595	$U_{west}$	(m s <sup>-1</sup> )	West wind component
596	$x$	(m)	lateral distance – approximately cross-wind
597	$x_L$	(m)	left half of the transect ( $x < x_{max}/2$ )
598	$x_{max}$	(m)	length of a transect
599	$x_R$	(m)	right half of the transect ( $x > x_{max}/2$ )



600	$y$	(m)	lateral distance – approximately co-wind
601	$z$	(m)	altitude
602	$\Phi_L(C)$	(-)	concentration probability distribution for left side of transect
603	$\Phi_R(C)$	(-)	concentration probability distribution for right side of transect
604	$\Phi_P(C)$	(-)	concentration probability distribution for the plume
605	$\Phi_B(C)$	(-)	concentration probability distribution for the background
606	$\alpha, \alpha'$	(-)	designation for Delano – Alta Sierra surface transect
607	$\varepsilon, \varepsilon'$	(-)	designation for Edison– Breckenridge Mtn. surface transect
608	$\tau, \tau'$	(-)	designation for Breckenridge – Caliente surface transect
609	$\beta, \beta', \beta_1'$	(-)	designation for Wasco – Granite surface transect
610	$\gamma, \gamma'$	(-)	designation for Oildale – Oil City surface and airborne transects
611	$\delta, \delta'$	(-)	designation for Ming Park – Arvin surface and airborne transects

612

613 **Data Availability.** Data will be provided as per the data policy.

614

615 **Author Contribution.** I. Leifer prepared the manuscript with input from all co-authors. C. Melton  
 616 prepared figures and conducted data analysis. M. Fischer helped prepare the emissions budgets. J. Frash  
 617 helped with AMOG data collection. L. Iraci, J. Marrero, J-M. Ryoo, T. Tanaka, and E. Yates are part of  
 618 the AJAX team and worked to collect and analyze AJAX data.

619 There are no competing interests

620

621 **Acknowledgements:** We thank the NASA Earth Science Division, Research and Analysis Program, grant  
 622 NNX13AM21G. MLF was supported by a grant from the California Energy Commission's Natural  
 623 Gas Research Program to the Lawrence Berkeley National Laboratory under contract DE-AC02-  
 624 36605CH11231. AJAX data were collected under the AJAX project, which acknowledges the partnership  
 625 of H211, LLC and support from the Ames Research Center Director's funds.

626

## 627 6. References

628 American Lung Association: State of the Air, 2016, American Lung Association, Chicago, IL, 157 pp.,  
 629 2016.

630 Bao, J. W., Michelson, S. A., Persson, P. O. G., Djalalova. I.V., and Wilczak, J. M.: Observed and WRF-





- 631 simulated low-level winds in a high-ozone episode during the Central California Ozone Study,  
632 *Journal of Applied Meteorology and Climatology*, 47, 2372-2394, 2008.
- 633 Boucouvala, D. and Bornstein, R.: Analysis of transport patterns during an SCOS97-NARSTO episode,  
634 *Atmospheric Environment*, 37, Supplement 2, 73-94, 2003.
- 635 Brandt, A. R., Heath, G. A., Kort, E. A., O'Sullivan, F., Pétron, G., Jordaan, S. M., Tans, P., Wilcox, J.,  
636 Gopstein, A. M., Arent, D., Wofsy, S., Brown, N. J., Bradley, R., Stucky, G. D., Eardley, D., and  
637 Harriss, R.: Methane leaks from North American natural gas systems, *Science*, 343, 733-735, 2014.
- 638 Bruhwiler, L. M., Basu, S., Bergamaschi, P., Bousquet, P., Dlugokencky, E., Houweling, S., Ishizawa,  
639 M., Kim, H. S., Locatelli, R., Maksyutov, S., Montzka, S., Pandey, S., Patra, P. K., Petron, G.,  
640 Saunio, M., Sweeney, C., Schwietzke, S., Tans, P., and Weatherhead, E. C.: US CH<sub>4</sub> emissions from  
641 oil and gas production: Have recent large increases been detected?, *Journal of Geophysical Research:*  
642 *Atmospheres*, doi: 10.1002/2016JD026157, 2017. 2016JD026157, 2017.
- 643 CALGEM: California Greenhouse Gas Emissions Measurement (CALGEM) Project. DOE, 2014.
- 644 CARB: Facility GHG Emissions Visualization and Analysis Tool: 2008-2014. California Environmental  
645 Protection Agency, Air Resources Board, 2016.
- 646 Chen, H., Winderlich, J., Gerbig, C., Hofer, A., Rella, C. W., Crosson, E. R., Van Pelt, A. D., Steinbach,  
647 J., Kolle, O., Beck, V., Daube, B. C., Gottlieb, E. W., Chow, V. Y., Santoni, G. W., and Wofsy, S. C.:  
648 High-accuracy continuous airborne measurements of greenhouse gases (CO<sub>2</sub> and CH<sub>4</sub>) using the  
649 cavity ring-down spectroscopy (CRDS) technique, *Atmos. Meas. Tech.*, 3, 375-386, 2010.
- 650 Dlugokencky, E. J., Croftwell, A., Masarie, K., White, J., Lang, P., and Croftwell, M.: NOAA  
651 Measurements of Long-lived Greenhouse Gases, *Asia-Pacific GAW Greenhouse Gases*, 6, 6-9, 2013.
- 652 EPA: 2013 Inventory of US greenhouse gas: Emissions and sinks: 1990-2011, Environmental Protection  
653 Agency, Washington DC, 457 pp., 2013.
- 654 EPA: 2017 Inventory of US greenhouse gas: Emissions and sinks: 1990-2015, Environmental Protection  
655 Agency, Washington DC430-P-17-001, 633 pp., 2017.
- 656 European Commission: Emission Database for Global Atmospheric Research (EDGAR). Joint Research  
657 Centre (JRC)/Netherlands Environmental Assessment Agency (PBL), 2010.
- 658 Farrell, P., Leifer, I., and Culling, D.: Transcontinental methane measurements: Part 1. A mobile surface  
659 platform for source investigations, *Atmospheric Environment*, 74, 422-431, 2013.
- 660 Fernandez-Cortes, A., Cuezva, S., Alvarez-Gallego, M., Garcia-Anton, E., Pla, C., Benavente, D., Jurado,  
661 V., Saiz-Jimenez, C., and Sanchez-Moral, S.: Subterranean atmospheres may act as daily methane  
662 sinks, *Nature Communication*, 6, 2015.
- 663 Gentner, D. R., Ford, T. B., Guha, A., Boulanger, K., Brioude, J., Angevine, W. M., de Gouw, J. A.,  
25



- 664 Warneke, C., Gilman, J. B., Ryerson, T. B., Peischl, J., Meinardi, S., Blake, D. R., Atlas, E.,  
665 Lonneman, W. A., Kleindienst, T. E., Beaver, M. R., Clair, J. M. S., Wennberg, P. O., VandenBoer,  
666 T. C., Markovic, M. Z., Murphy, J. G., Harley, R. A., and Goldstein, A. H.: Emissions of organic  
667 carbon and methane from petroleum and dairy operations in California's San Joaquin Valley,  
668 *Atmospheric Chemistry and Physics*, 14, 4955-4978, 2014.
- 669 Ghosh, A., Patra, P. K., Ishijima, K., Umezawa, T., Ito, A., Etheridge, D. M., Sugawara, S., Kawamura,  
670 K., Miller, J. B., Dlugokencky, E. J., Krummel, P. B., Fraser, P. J., Steele, L. P., Langenfelds, R. L.,  
671 Trudinger, C. M., White, J. W. C., Vaughn, B., Saeki, T., Aoki, S., and Nakazawa, T.: Variations in  
672 global methane sources and sinks during 1910–2010, *Atmospheric Chemistry and Physics*, 15, 2595-  
673 2612, 2015.
- 674 Hamill, P., Iraci, L. T., Yates, E. L., Gore, W., Bui, T. P., Tanaka, T., and Loewenstein, M.: A new  
675 instrumented airborne platform for atmospheric research, *Bulletin of the American Meteorological*  
676 *Society*, 97, 2015.
- 677 IPCC: *Climate Change 2007: Synthesis Report. Contribution of Working Groups I, II, and III to the*  
678 *Fourth Assessment Report of the Intergovernmental Panel on Climate Change*, IPCC, Geneva,  
679 Switzerland, 104 pp., 2007.
- 680 IPCC: *Working Group 1 Contribution to the IPCC Fifth Assessment Report Climate Change 2013-The*  
681 *Physical Science Basis*, International Panel on Climate Change, IPCC Secretariat, Geneva,  
682 Switzerland, 2216 pp., 2013.
- 683 Jeong, S., Hsu, Y.-K., Andrews, A. E., Bianco, L., Vaca, P., Wilczak, J. M., and Fischer, M.: Multi-tower  
684 measurement network estimate of California's methane emissions, *Journal of Geophysical Research -*  
685 *Atmospheres*, 118, 2013JD019820, 2013.
- 686 Jeong, S., Zhao, C., Andrews, A. E., Bianco, L., Wilczak, J. M., and Fischer, M. L.: Seasonal variation of  
687 CH<sub>4</sub> emissions from central California, *Journal of Geophysical Research*, 117, 2012.
- 688 Jeong, S. S., Millstein, D., and Fischer, M. L.: Spatially explicit methane emissions from petroleum  
689 production and the natural gas system in California, *Environmental Science & Technology*, 48, 5982-  
690 5990, 2014.
- 691 John, J. G., Fiore, A. M., Naik, V., Horowitz, L. W., and Dunne, J. P.: Climate versus emission drivers of  
692 methane lifetime against loss by tropospheric OH from 1860–2100, *Atmospheric Chemistry and*  
693 *Physics*, 12, 12021-12036, 2012.
- 694 Karion, A., Sweeney, C., Pétron, G., Frost, G., Michael Hardesty, R., Kofler, J., Miller, B. R., Newberger,  
695 T., Wolter, S., Banta, R., Brewer, A., Dlugokencky, E., Lang, P., Montzka, S. A., Schnell, R., Tans,  
696 P., Trainer, M., Zamora, R., and Conley, S.: Methane emissions estimate from airborne measurements



- 697 over a western United States natural gas field, *Geophysical Research Letters*, 40, 4393-4397, 2013.
- 698 Karlisdóttir, S. and Isaksen, I. S. A.: Changing methane lifetime: Possible cause for reduced growth,  
699 *Geophysical Research Letters*, 27, 93-96, 2000.
- 700 Khalil, M. A. K. and Rasmussen, R. A.: The changing composition of the Earth's atmosphere. In:  
701 *Composition, chemistry, and climate of the atmosphere*, Singh, H. B. (Ed.), Van Nostrand Reinhold,  
702 New York, 1995.
- 703 Kirschke, S., Bousquet, P., Ciais, P., Saunois, M., Canadell, J. G., Dlugokencky, E. J., Bergamaschi, P.,  
704 Bergmann, D., Blake, D. R., and Bruhwiler, L.: Three decades of global methane sources and sinks,  
705 *Nature Geoscience*, 6, 813-823, 2013.
- 706 Krautwurst, S., Gerilowski, K., Krings, T., Borchard, J., Bovensmann, H., Leifer, I., Fladland, M. M.,  
707 Koyler, R., Iraci, L. T., Luna, B., Thompson, D. R., Eastwood, M., Green, R., Jonsson, H. H., Vigil,  
708 S. A., and Tratt, D. M.: COMEX - Final Report: Scientific and Technical Assistance for the  
709 Deployment of a flexible airborne spectrometer system during CMAPEXP and COMEX, IUP-  
710 COMEX-FR, 148 pp., 2016.
- 711 Krings, T., Gerilowski, K., Buchwitz, M., Reuter, M., Tretner, A., Erzinger, J., Heinze, D., Pflüger, U.,  
712 Burrows, J. P., and Bovensmann, H.: MAMAP – a new spectrometer system for column-averaged  
713 methane and carbon dioxide observations from aircraft: Retrieval algorithm and first inversions for  
714 point source emission rates, *Atmospheric Measurement Techniques*, 4, 1735-1758, 2011.
- 715 LaFranchi, B. W., Pétron, G., Miller, J. B., Lehman, S. J., Andrews, A. E., Dlugokencky, E. J., Hall, B.,  
716 Miller, B. R., Montzka, S. A., Neff, W., Novelli, P. C., Sweeney, C., Turnbull, J. C., Wolfe, D. E.,  
717 Tans, P. P., Gurney, K. R., and Guilderson, T. P.: Constraints on emissions of carbon monoxide,  
718 methane, and a suite of hydrocarbons in the Colorado Front Range using observations of  $^{14}\text{CO}_2$ ,  
719 *Atmos. Chem. Phys.*, 13, 11101-11120, 2013.
- 720 Lamb, B. K., McManus, J., Shorter, J., Kolb, C., Mosher, B., Harriss, R., Allwine, E., Blaha, D., Howard,  
721 T., Guenther, A., Lott, R., Siverson, R., Westburg, H., and Zimmerman, P.: Development of  
722 atmospheric tracer methods to measure methane emissions from natural gas facilities and urban areas,  
723 *Environmental Science & Technology*, 29, 1468-1479, 1995.
- 724 Leen, J. B., Yu, X. Y., Gupta, M., Baer, D. S., Hubbe, J. M., Kluzek, C. D., Tomlinson, J. M., and  
725 Hubbell, M. R., 2nd: Fast in situ airborne measurement of ammonia using a mid-infrared off-axis  
726 ICOS spectrometer, *Environmental Science & Technology*, 47, 10446-10453, 2013.
- 727 Leifer, I., Culling, D., Schneising, O., Farrell, P., Buchwitz, M., and Burrows, J.: Transcontinental  
728 methane measurements: Part 2. Mobile surface investigation of fossil fuel industrial fugitive  
729 emissions, *Atmospheric Environment*, 74, 432-441, 2013.



- 730 Leifer, I., Melton, C., Manish, G., and Leen, B.: Mobile monitoring of methane leakage, Gases and  
731 Instrumentation, July/August 2014, 20-24, 2014.
- 732 Lillis, P. G., Warden, A., Claypool, G. E., and Magoon, L. B.: Petroleum systems of the San Joaquin  
733 Basin Province -- geochemical characteristics of gas types: Chapter 10. In: Petroleum systems and  
734 geologic assessment of oil and gas in the San Joaquin Basin Province, California, Scheirer, A. H.  
735 (Ed.), 1713-10, U. S. Geological Survey, Reston, VA, 2008.
- 736 McKain, K., Down, A., Raciti, S. M., Budney, J., Hutyra, L. R., Floerchinger, C., Herndon, S. C.,  
737 Nehrkorn, T., Zahniser, M. S., Jackson, R. B., Phillips, N., and Wofsy, S. C.: Methane emissions  
738 from natural gas infrastructure and use in the urban region of Boston, Massachusetts, Proceedings of  
739 the National Academy of Sciences, 2015. 2015.
- 740 Meyers, M. P. and Steenburgh, W. J.: Mountain Weather Prediction: Phenomenological Challenges and  
741 Forecast Methodology. In: Mountain Weather Research and Forecasting: Recent Progress and  
742 Current Challenges, Chow, K. F., De Wekker, F. J. S., and Snyder, J. B. (Eds.), Springer Netherlands,  
743 Dordrecht, 2013.
- 744 Miller, S. M., Wofsy, S. C., Michalak, A. M., Kort, E. A., Andrews, A. E., Biraud, S. C., Dlugokencky, E.  
745 J., Eluszkiewicz, J., Fischer, M. L., Janssens-Maenhout, G., Miller, B. R., Miller, J. B., Montzka, S.  
746 A., Nehrkorn, T., and Sweeney, C.: Anthropogenic emissions of methane in the United States,  
747 Proceedings of the National Academy of Sciences, 110, 20018-20022, 2013.
- 748 NASA: <https://www.nasa.gov/image-feature/goddard/wildfires-in-california-august-17-2015>, last access: 16  
749 April 2017, 2015.
- 750 Nisbet, E. G., Dlugokencky, E. J., and Bousquet, P.: Methane on the Rise—Again, Science, 343, 493-495,  
751 2015.
- 752 Peischl, J., Ryerson, T. B., Aikin, K. C., de Gouw, J. A., Gilman, J. B., Holloway, J. S., Lerner, B. M.,  
753 Nadkarni, R., Neuman, J. A., Nowak, J. B., Trainer, M., Warneke, C., and Parrish, D. D.: Quantifying  
754 atmospheric methane emissions from the Haynesville, Fayetteville, and northeastern Marcellus shale  
755 gas production regions, Journal of Geophysical Research: Atmospheres, 120, 2119-2139, 2015.
- 756 Peischl, J., Ryerson, T. B., Brioude, J., Aikin, K. C., Andrews, A. E., Atlas, E., Blake, D., Daube, B. C.,  
757 de Gouw, J. A., Dlugokencky, E., Frost, G. J., Gentner, D. R., Gilman, J. B., Goldstein, A. H., Harley,  
758 R. A., Holloway, J. S., Kofler, J., Kuster, W. C., Lang, P. M., Novelli, P. C., Santoni, G. W., Trainer,  
759 M., Wofsy, S. C., and Parrish, D. D.: Quantifying sources of methane using light alkanes in the Los  
760 Angeles basin, California, Journal of Geophysical Research: Atmospheres, 118, n/a-n/a, 2013.
- 761 Pétron, G., Frost, G., Miller, B. R., Hirsch, A. I., Montzka, S. A., Karion, A., Trainer, M., Sweeney, C.,  
762 Andrews, A. E., Miller, L., Kofler, J., Bar-Ilan, A., Dlugokencky, E. J., Patrick, L., Moore, C. T. J.,



- 763 Ryerson, T. B., Siso, C., Kolodzey, W., Lang, P. M., Conway, T., Novelli, P., Masarie, K., Hall, B.,  
764 Guenther, D., Kitzis, D., Miller, J., Welsh, D., Wolfe, D., Neff, W., and Tans, P.: Hydrocarbon  
765 emissions characterization in the Colorado Front Range: A pilot study, *J. Geophys. Res.*, 117,  
766 D04304, 2012.
- 767 Rigby, M., Prinn, R. G., Fraser, P. J., Simmonds, P. G., Langenfelds, R. L., Huang, J., Cunnold, D. M.,  
768 Steele, L. P., Krummel, P. B., Weiss, R. F., O'Doherty, S., Salameh, P. K., Wang, H. J., Harth, C. M.,  
769 Mühle, J., and Porter, L. W.: Renewed growth of atmospheric methane, *Geophys. Res. Lett.*, 35,  
770 L22805, 2008.
- 771 Simpson, I. J., Sulbaek Andersen, M. P., Meinardi, S., Bruhwiler, L., Blake, N. J., Helmig, D., Rowland,  
772 F. S., and Blake, D. R.: Long-term decline of global atmospheric ethane concentrations and  
773 implications for methane, *Nature*, 488, 490-494, 2012.
- 774 Sonnemann, G. R. and Grygalashvyly, M.: Global annual methane emission rate derived from its current  
775 atmospheric mixing ratio and estimated lifetime, *Annales Geophysicae*, 32, 277-283, 2014.
- 776 Sun, K., Tao, L., Miller, D. J., Khan, A. M., and Zondlo, M. A.: On-road ammonia emissions  
777 characterized by mobile, open-path measurements, *Environmental Science & Technology*, 48, 3943-  
778 3950, 2014.
- 779 Tanaka, T., Yates, E., Iraci, L. T., Johnson, M. S., Gore, W., Tadi, J. M., Loewenstein, M., Kuze, A.,  
780 Frankenberg, C., Butz, A., and Yoshida, Y.: Two-year comparison of airborne measurements of  
781 CO<sub>2</sub> and CH<sub>4</sub> with GOSAT at Railroad Valley, Nevada, *IEEE*  
782 *Transactions on Geoscience and Remote Sensing*, 54, 4367-4375, 2016.
- 783 Thompson, D., Leifer, I., Bovensman, H., Eastwood, M., Fladeland, M., Frankenberg, C., Gerilowski, K.,  
784 Green, R., Krautwurst, S., Krings, T., Luna, B., and Thorpe, A. K.: Real-time remote detection and  
785 measurement for airborne imaging spectroscopy: A case study with methane, *Atmospheric*  
786 *Measurement Techniques*, 8, 1-46, 2015.
- 787 Turner, A. J., Jacob, D. J., Benmergui, J., Wofsy, S. C., Maasackers, J. D., Butz, A., Hasekamp, O., and  
788 Biraud, S. C.: A large increase in U.S. methane emissions over the past decade inferred from satellite  
789 data and surface observations, *Geophysical Research Letters*, 43, 2218-2224, 2016.
- 790 VanCuren, R.: Transport aloft drives peak ozone in the Mojave Desert, *Atmospheric Environment*, 109,  
791 331-341, 2015.
- 792 Wennberg, P. O., Mui, W., Wunch, D., Kort, E. A., Blake, D. R., Atlas, E. L., Santoni, G. W., Wofsy, S.  
793 C., Diskin, G. S., Jeong, S., and Fischer, M. L.: On the sources of methane to the Los Angeles  
794 atmosphere, *Environmental Science & Technology*, 46, 9282-9289, 2012.
- 795 White, W. H., Anderson, J. A., Blumenthal, D. L., Husar, R. B., Gillani, N. V., Husar, J. D., and Wilson,  
29



- 796 W. E.: Formation and transport of secondary air pollutants: Ozone and aerosols in the St. Louis urban  
797 plume, *Science*, 194, 187-189, 1976.
- 798 Wunch, D., Wennberg, P. O., Toon, G. C., Keppel-Aleks, G., and Yavin, Y. G.: Emissions of greenhouse  
799 gases from a North American megacity, *Geophysical Research Letters*., 36, 2009.
- 800 Yacovitch, T. I., Herndon, S. C., Pétron, G., Kofler, J., Lyon, D., Zahniser, M. S., and Kolb, C. E.: Mobile  
801 laboratory observations of methane emissions in the Barnett Shale Region, *Environmental Science &*  
802 *Technology*, 49, 7889-7895, 2015.
- 803 Yates, E. L., Iraci, L. T., Roby, M. C., Pierce, R. B., Johnson, M. S., Reddy, P. J., Tadić, J. M.,  
804 Loewenstein, M., and Gore, W.: Airborne observations and modeling of springtime stratosphere-to-  
805 troposphere transport over California, *Atmospheric Chemistry Physics*, 13, 12481-12494, 2013.
- 806 Zhong, S., Whiteman, C. D., and Bian, X.: Diurnal evolution of three-dimensional wind and temperature  
807 structure in California's Central Valley, *Journal of Applied Meteorology*, 43, 1679-1699, 2004.